Heliospheric Structure as Revealed by the 3–88 keV H ENA Spectra

A. Czechowski[1], M. Bzowski[1], J. M. Sokół[1], M. A. Kubiak[1], J. Heerikhuisen[2], E. J. Zirnstein[3], N. V. Pogorelov[2], N. A. Schwadron[4], M. Hilchenbach[5], J. Grygorczuk[1], and G. P. Zank[2]

[1] Space Research Centre PAS (CBK PAN), Bartycka 18 A, 00-716 Warsaw, Poland; bzowski@cbk.waw.pl
[2] Department of Space Science and Center for Space Plasma and Aeronomic Research, University of Alabama in Huntsville, Huntsville, AL, USA
[3] Department of Astrophysical Sciences, Princeton University, Princeton, NJ, USA
[4] Space Science Center and Department of Physics, University of New Hampshire, Durham, NH, USA
[5] Max-Planck-Institut für Sonnensystemforschung, Göttigen, Germany

Abstract

Energetic neutral atoms (ENAs) are an important tool for investigating the structure of the heliosphere. Recently, it was observed that fluxes of ENAs (with energy ⩽55 keV) coming from the upwind and downwind regions of the heliosphere are similar in strength. This led the authors of these observations to hypothesize that the heliosphere is bubble-like rather than comet-like, meaning that it has no extended tail. We investigate the directional distribution of the ENA flux for a wide energy range (3–88 keV) including observations from *IBEX* (*Interstellar Boundary Explorer*), INCA (Ion and Neutral Camera, on board *Cassini*), and HSTOF (High-energy Suprathermal Time Of Flight sensor, on board the *Solar and Heliospheric Observatory*). An essential element is the model of pickup ion (PUI) acceleration at the termination shock proposed by Zank. We use state-of-the-art models of the global heliosphere, interstellar neutral gas density, and PUI distributions. The results, based on the "comet-like" model of the heliosphere, are close in flux magnitude to ENA observations by *IBEX*, HSTOF, and partly those by INCA (except for the 5.2–13.5 keV energy channel). We find that the ENA flux from the tail dominates at high energy (in agreement with HSTOF, but not INCA). At low energy, our comet-like model produces ENA fluxes of similar strength from the upwind and downwind directions—which, therefore, removes this as a compelling argument for a bubble-like heliosphere.

Unified Astronomy Thesaurus concepts: Solar physics (1476); Solar wind (1534); Heliopause (707); Interplanetary physics (827); Pickup ions (1239); Solar wind termination (1535); Heliosphere (711); Interplanetary particle acceleration (826)

1. Introduction

The energetic neutral atoms (ENAs) considered in this work are created due to multistage processing of interstellar neutral (ISN) atoms inside the heliosphere. Unlike interstellar ions, ISN atoms freely penetrate deep inside the termination shock (TS), where some of them are ionized by photoionization and charge exchange with protons from the solar wind (SW). The ionized ISN atoms form a suprathermal subpopulation of the SW, known as pickup ions (PUIs; Holzer & Axford 1971; Vasyliunas & Siscoe 1976). Due to a sequence of interactions with the TS, some of the PUIs are accelerated to energies of dozens of keV and larger before being convected into the inner heliosheath, i.e., the region of SW plasma between the TS and heliopause (HP; Lee et al. 1996; Zank et al. 1996, 2010; Kumar et al. 2018). In the inner heliosheath, the PUIs maintain their suprathermal energy and flow with the shocked SW plasma until they are converted into ENAs by neutralization, predominantly through resonant charge exchange with ISN H atoms that have penetrated inside the HP. These ENAs propagate freely in all directions, carrying information about the ion distributions in their inner heliosheath source region.

The observation of ENAs is presently one of the most important means for diagnosing the global heliosphere (Gruntman 1997). The motion of the Sun relative to the interstellar medium affects the distribution of the primordial seed population of ENAs, i.e., the ISN atoms inside the TS, and consequently the production of PUIs. The acceleration of PUIs to ENA energies and their transport downstream of the shock are determined by the heliospheric plasma flow geometry. Therefore, to understand the relationship between the ENA flux

distribution and the structure of the heliosphere, we must harness theoretical models of: (1) the ISN H distribution and the production of PUIs inside TS; (2) the plasma flow in the inner heliosheath, where the heliospheric ENAs observed at Earth's orbit are produced; and (3) the PUI distribution at the TS and its evolution as it is convected through the heliosheath.

At present, theoretical models of the heliosphere give only an approximate picture. In particular, the thickness of the inner heliosheath (an important parameter for the ENA distribution) is overestimated by all MHD and MHD-kinetic numerical solutions. Moreover, *Voyager* observations at the TS imply that the highly nonthermal ion component has a large effect on plasma dynamics in this region—an effect not yet fully taken into account in most state-of-art models. Therefore, we cannot aim at a precise modeling of the ENA distribution while following theoretical models uncritically.

Altogether, we address the following topics:

(A) The energy spectrum and directional distribution of the hydrogen ENAs over a wide energy range, including the high-energy (above ∼40 keV) ENA. This permits us to link with the *Voyager* Low Energy Charged Particle (LECP) energetic ion measurements (E ⩾ 28 keV for V1 and E ⩾ 40 keV for V2) and test the theoretical model of the flux intensity and the energy spectrum of the pick-up ions at the TS proposed by Zank et al. (1996, 2010). The energy range extends from 3 keV (the highest bin of *IBEX* High) to 88 keV (maximum energy of HSTOF) and includes the observations by INCA.
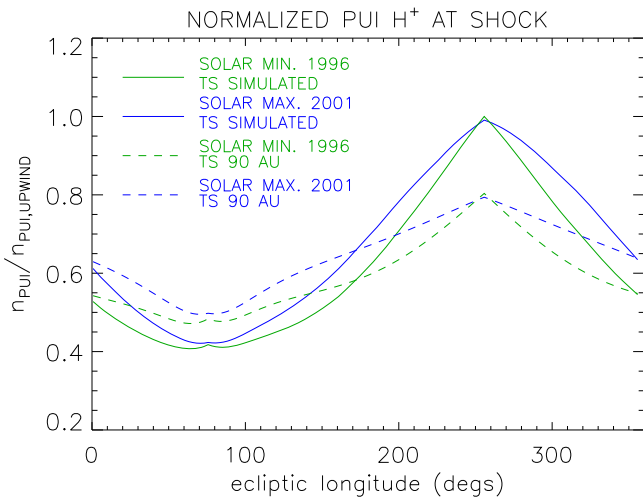
Figure 1. Variation of the normalized H$^+$ PUI density along the TS in the ecliptic plane, following the nWTPM model. Solid lines correspond to the TS location derived from the Huntsville model, and dashed lines to the hypothetical case of the Sun-centered spherical TS with a radius of 90 au. For all the curves of the same kind, the density is normalized to the same upwind value (longitude 255°) during the 1996 solar minimum. The PUI-normalized density distribution is weakly sensitive to the phase of the solar cycle (green vs. blue), but much more sensitive to the geometry of the TS (solid vs. dashed). The absolute values of the PUI density along the TS are different for the spherical Sun-centered and the simulated shock locations.

(B) Tail/nose asymmetry of the ENA flux in the heliosphere, in particular the energy dependence of the tail/nose ENA flux ratio. Our aim here is to find out to what extent this ratio can be regarded as a signature of the heliosphere with an extended tail, i.e., the "comet-like" heliosphere (Parker 1961; Baranov et al. 1991). In the present work, we do not employ a fully time-dependent model of the heliosphere, so we cannot discuss the important issue of time dependence of the ENA flux coming from the tail direction (Dialynas et al. 2017). However, this topic was recently addressed by Schwadron & Bzowski (2018).

We restrict our simulations to the vicinity of the ecliptic plane, to stay within the observation region of the High-energy Suprathermal Time Of Flight sensor (HSTOF) on board *SOHO* (*Solar and Heliospheric Observatory*).

Our simulations are organized as follows. The locations of the TS and the HP and the plasma flow in the inner heliosheath are taken from the time-stationary Huntsville model of the heliosphere (Heerikhuisen & Pogorelov 2010), run with the best currently known parameters of interstellar gas populations (Bzowski et al. 2015; McComas et al. 2015; Kubiak et al. 2016), and the interstellar magnetic field (Frisch et al. 2015; Zirnstein et al. 2016). The Huntsville model does not explicitly include a separate PUI component; the plasma fluid in the simulation should be considered as a bulk SW and PUI mixture.

We start from the hot model of ISN H distribution inside the heliosphere (Tarnopolski & Bzowski 2009), using an observation-based model of the time and latitude evolution of the radiation pressure (Kowalska-Leszczynska et al. 2018a), the photoionization rate (Bzowski et al. 2013b), and the SW speed and density (Sokół et al. 2013), needed to calculate the charge-exchange ionization rate. From the simulated ISN H distribution between the Sun and the TS, we calculate the density of PUIs arriving at the TS in the ecliptic plane (Sokół et al. 2019b) for two selected
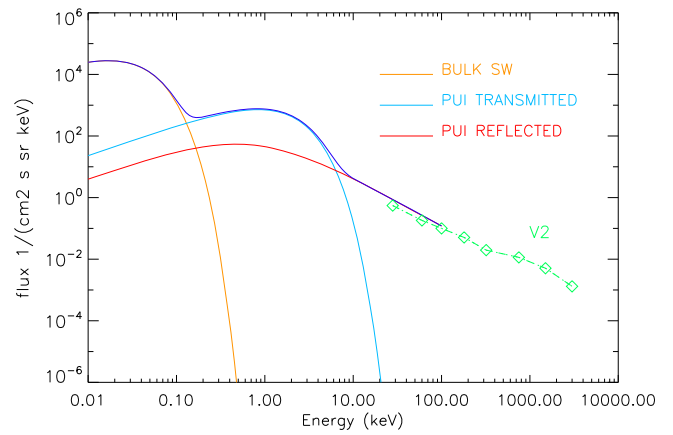

Figure 2. Simulated energetic proton spectrum downstream from the TS obtained via the model of Zank et al. (2010) for the shock parameters as observed by *Voyager* 2, compared with *Voyager* 2/LECP $Z \geqslant 1$ ions measurements (Giacalone & Decker 2010). Simulated spectrum is a super-position of two Maxwell–Boltzmann functions for the bulk SW and transmitted PUI populations, and a kappa function with $\kappa = 1.6$ for the reflected PUI population. Dark blue line is the sum of all components.

phases of the solar cycle (Figure 1). The parameters chosen for this model are presented in Appendix A.

As a next step, we use the Zank acceleration theory of the transmission and reflection of PUI components at the TS to obtain the PUI spectra just beyond the TS (Zank et al. 1996, 2010). The example of the proton spectrum corresponding to the TS parameters encountered by *Voyager* 2 is shown in Figure 2, with contributions of the bulk SW protons and of the transmitted and reflected PUIs. We then follow the convection and gradual decharging of these ions as they propagate within the IHS plasma. We use the heliosheath distribution of ISN H, the TS location, and the plasma flow from the Huntsville heliosphere model.

The TS transition observed by *Voyager* 2 consisted of a narrow subshock and an extended (0.7 au) precursor (Florinski et al. 2009). In the Huntsville model, where the plasma is treated as a single fluid, this transition appears as a single shock, with the strength combining the subshock and the precursor strengths. To apply the Zank et al. theory, we have to estimate the strength of the subshock. We make a simple assumption that the subshock strength is lower than the shock strength in the Huntsville model by a constant fraction. Its value (0.68) is chosen by the requirement that the resulting subshock strength at the point of *Voyager* 2 crossing the simulated shock is equal to the TS strength determined from *Voyager* 2 observations.

Finally, we simulate the ENA flux along the ecliptic plane in the energy bands corresponding to *IBEX* (*Interstellar Boundary Explorer*), INCA (Ion and Neutral Camera, on board *Cassini*), and HSTOF measurements. The comparison of the simulated ENA flux with the observations by *IBEX* (3–6 keV, midpoint 4.3 keV) (Schwadron et al. 2014b), by INCA (at 5.2–13.5 keV and 35–55 keV) (Dialynas et al. 2017), and by HSTOF (58–88 keV) (Hilchenbach et al. 1998; Czechowski et al. 2006) is presented in Figure 3 (tail and nose directions) and Figure 4 (all directions near the ecliptic). Figure 3 includes an additional data point for *IBEX* (2–3.8 keV, midpoint 2.7 keV).

A detailed description of the models used in our simulations is given in Sections 2–5. Specifically, Section 2 presents the global model of the heliosphere, Section 3 our method of
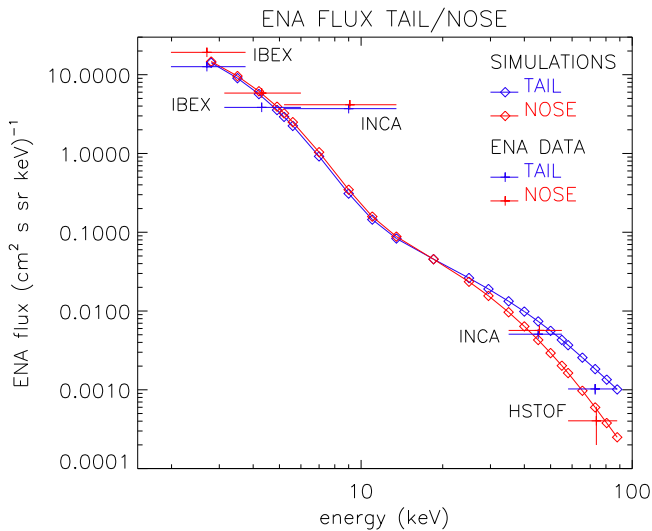
Figure 3. Simulated H ENA spectrum from the tail and the nose directions, compared with observations by *IBEX* (2.7 and 4.3 keV), INCA (5.2–13.5 keV and 35–55 keV), and HSTOF (58–88 keV). An antisunward-looking observer is located at 1 au. The ENA data are the same as in Figure 4, averaged in ecliptic longitude over the nose $255° ± 25°$ and the tail $75° ± 25°$ regions, respectively. Horizontal bars correspond to the energy ranges of the observations; vertical bars are the measurement uncertainties estimates. For the *IBEX* data points, the vertical bars do not represent the errors, which are too small to visualize. Simulated spectra from the tail and the nose regions agree with each other for the energies up to ∼20 keV (simulations) or ∼40 keV (observations), and diverge for higher energies. This divergence can be explained by the rapid fall-off in the charge-exchange cross section at high energy, which effectively extends the production region of high-energy ENAs in the heliotail. Note that the only measurement that markedly differs from the model ENA spectrum, and also from the observed *IBEX* Hi spectrum, is the INCA 5.2–13.5 keV range.

obtaining the pick-up protons density distribution upstream of the TS, Section 4 the theory of acceleration of PUIs at the TS and the resulting energetic ion spectra, and Section 5 the conversion of the energetic protons to ENAs. Section 6 provides information about the ENA flux data used in this work. Our results and conclusions are summarized in Section 7. In Appendix A, we include more details about the parameters of the interstellar medium and the heliosphere. Appendix B describes the toy model of the ENA tail/nose flux ratio. In Appendix C, we present some MHD+neutral models of the heliosphere with two-funnel topology, corresponding to the case of strong interstellar magnetic field.

2. Model of the Heliosphere

The locations of the TS and the HP and the plasma flow in between are obtained from the time-stationary Huntsville model. The model combines an MHD description of the interaction of solar and interstellar plasmas with a kinetic description of neutral hydrogen atoms (Pogorelov et al. 2008; Heerikhuisen & Pogorelov 2010). The SW and interstellar plasmas are described as a single fluid under ideal MHD equations. The MHD equations are coupled to neutral hydrogen through mass, momentum, and energy source terms via photoionization and charge-exchange. The Boltzmann equation is solved using a Monte Carlo approach in order to solve for the neutral hydrogen distribution in phase space. We use the MHD solution for (1) estimating the TS distances, (2) retrieving the neutral H density in the heliosheath, and (3) retrieving the plasma streamlines in the heliosheath. The other information
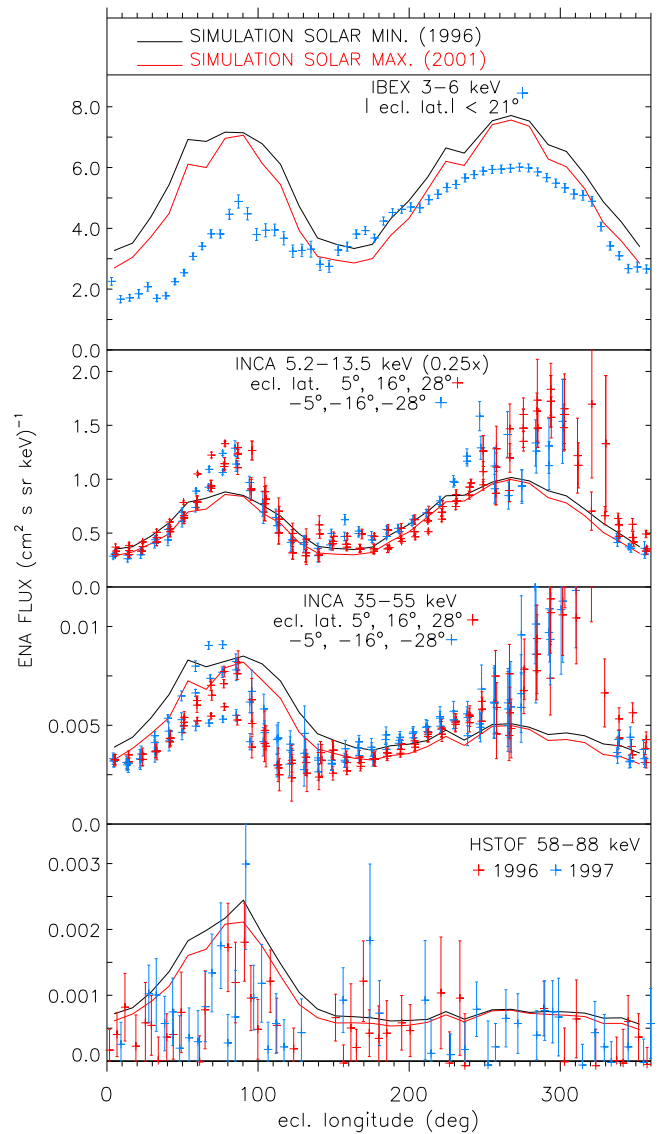

Figure 4. Simulated H ENA flux near the ecliptic plane compared with observations. In the second panel (the INCA 5.2–13.5 keV data), the observed flux was scaled down by a factor 0.25 to facilitate comparison with the simulations. The H ENA flux was observed by *IBEX* (Schwadron et al. 2014a) between 2009 and 2014, INCA in two energy bands (digitized from Figure 3(a) in Dialynas et al. 2017), and HSTOF (Czechowski et al. 2006). The simulations, averaged over the energy ranges of the measurements, were done using the (time-stationary) Huntsville model of the heliosphere together with the nWTPM model results for the PUI distribution during the solar minimum (black) and maximum (red) conditions. The INCA data, gathered between 2003 and 2014, correspond to a range of latitudes, both above (red) and below (blue) the ecliptic plane. The HSTOF data come from the first two years of operation, with favorable observing conditions: 1996 (red) and 1997 (blue).

needed for our simulations is derived from the nWTPM model for the neutral H, the model of the PUI distribution upstream from TS (Sokół et al. 2019b), and the Zank's theory for the PUI temperatures across the shock.

The boundary conditions for the model are specified as follows. At 1 au, the SW plasma density is $5.74 \, \text{cm}^{-3}$, temperature is 51,100 K, flow speed is 450 km s^{-1}, and the magnetic field radial component is 37.5 μG, all independent of heliolatitude. These values are then advected to the simulation's inner boundary at 10 au, assuming adiabatic expansion. Neutral hydrogen atoms generated in the heliosphere outside of

the TS are adopted in our calculation directly from the Huntsville model, assuming a kappa distribution for the plasma in the inner heliosheath and a Maxwell–Boltzmann distribution outside the HP.

In the unperturbed Very Local Interstellar Matter (VLISM), the strength of magnetic field was adopted as 2.93 μG, pointing toward ecliptic (longitude, latitude)=(227°.28, 34°.62) (Zirnstein et al. 2016). The VLISM temperature and speed adopted were 7500 K and 25.4 km s^{-1}, respectively (McComas et al. 2015), the proton density 0.09 cm^{-3}, and the H density 0.154 cm^{-3} (Zirnstein et al. 2016).

Along the *Voyager* 1 (2) directions, the model gives a distance to the HP $r_{\rm HP}$ = 118 (115) au, and to the TS $R_{\rm TS}$ = 74 (74) au, implying the thickness of the inner heliosheath to be $L_{\rm IHS}$ = 44 (41) au. The observed values are 121 (119) au, 94 (84) au, and 27 (35) au, respectively.

During the past 25 yr, the SW flux featured a secular change (in addition to quasi-periodic solar cycle variations), with a gradual decrease between ~1990 and 2010, an increased plateau during 2010–2014, and a sharp increase in 2014; see, e.g., Figure 4 in Czechowski et al. (2018) and Figure 1 in McComas et al. (2018). This very likely resulted in significant changes to the structure of the heliosphere, in particular in the TS distance (depending on the location along the TS). To correctly estimate the thickness of the heliosheath from the *Voyager* 1 (2) measurements of the distance to TS in 2005 (2008) and to HP in 2012 (2018) requires taking this time-dependence into account.

3. Pick-up Protons' Density Upstream of TS

The parent ions of the ENAs considered in our simulation are the pick-up protons accelerated at the TS. To determine their distribution, we must know the density of the pick-up protons arriving at the TS with the SW.

Calculation of the PUI densities along the TS was done using the formula (Ruciński & Fahr 1991; Ruciński et al. 2003; Sokół et al. 2019b):

$$F_{\rm PUI}(\mathbf{r}_{\rm TS}, t) = \frac{1}{r_{\rm TS}^2(\boldsymbol{\omega})} \int_{r_0(\boldsymbol{\omega})}^{r_{\rm TS}(\boldsymbol{\omega})} n_{\rm H}(\mathbf{r}', t)\beta(\mathbf{r}', t)r'^2 dr', \quad (1)$$

where $n_{\rm H}$ is the density of ISN H for the time t at radius-vector $\mathbf{r}$ from the Sun, and β is the ionization rate of ISN H at radius-vector $\mathbf{r}'$ for a time t. The heliocentric radius vector $\mathbf{r}(r, \boldsymbol{\omega})$ is parameterized by its length r and direction (a directional unit vector $\boldsymbol{\omega}(\lambda, \phi)$, where (λ, ϕ) are ecliptic longitude and latitude). Note that β is for a solar distance r, not for 1 au, and that it varies with heliolatitude. The integration goes radially from a distance r_0 from the Sun to the TS distance $r_{\rm TS}$ along the direction $\boldsymbol{\omega}$. Assuming that PUIs propagate radially and the SW speed is independent of solar distance, the density of PUIs at TS is calculated as $n_{\rm PUI} = F_{\rm PUI}/v_{\rm SW}$. This calculation is an approximation where the slowdown of the SW due to momentum loading by newly injected PUIs and the effects of finite propagation time of SW from the Sun to the TS are neglected. A discussion of the validity of this approximation is provided by Bzowski et al. (2013b), pages 82–86.

The densities $n_{\rm H}$ were calculated adopting the paradigm of the classical hot model of the ISN H distribution in the heliosphere (Thomas 1978), with modifications to account for the dependence of the solar radiation pressure on time and

radial velocity due to the evolution of the solar Lyα emission profile with time (Tarnopolski & Bzowski 2009) and for the variation of the ionization rate with time and heliolatitude (Ruciński & Bzowski 1995; Bzowski 2003).

In the hot-model paradigm, the density of ISN H at a location given by a radius-vector $\mathbf{r}$ and time t is calculated by numerical integration of the local distribution functions of the primary and secondary populations $f_{\rm pri}$, $f_{\rm sec}$ over the three-dimensional velocity space (Baranov et al. 1998):

$$n_{\rm H}(\mathbf{r}, t) = n_{\rm H,pri}(\mathbf{r}, t) + n_{\rm H,sec}(\mathbf{r}, t)$$
$$= \int (f_{\rm pri}(\mathbf{v}, \mathbf{r}, t) + f_{\rm sec}(\mathbf{v}, \mathbf{r}, t))d\mathbf{v}. \quad (2)$$

These distribution functions strongly vary with time, distance to the Sun, and ecliptic coordinates. The local distribution function $f(\mathbf{v}, \mathbf{r}, t)$ is ballistically connected by atom trajectories with the distribution function of ISN H at the TS, assumed to be Maxwell–Boltzmann with the parameters discussed in Appendix A. The radiation pressure varies with time, heliolatitude, and radial speed of the atom along its trajectory. The model used here is from Kowalska-Leszczynska et al. (2018a). This results in different velocity vectors of the H atoms in their source region in the interstellar medium for identical velocities at $\mathbf{r}$ but for different times t. The ionization losses also vary between trajectories of different H atoms intersecting at the time t at $\mathbf{r}$. The atom velocity vectors in the interstellar medium and the ionization losses for individual trajectories are calculated by numerical integration of the respective quantities along the numerically tracked trajectories (see Section 2 in Bzowski et al. 2013a).

PUIs are produced due to ionization of ISN H by charge exchange with SW protons, by photoionization by solar EUV photons, and by electron-impact ionization, which all vary with the solar distance, heliolatitude, and time (Bzowski et al. 2013b; Sokół et al. 2019a):

$$\beta_{\rm ion}(\mathbf{r}, t) = \beta_{\rm prod}(\mathbf{r}, t)$$
$$= \beta_{\rm cx}(\mathbf{r}, t) + \beta_{\rm ph}(\mathbf{r}, t) + \beta_{\rm el}(\mathbf{r}, t). \quad (3)$$

The SW speed model (Sokół et al. 2013) used to calculate the charge-exchange and electron ionization rates was also used to compute the PUI flux and density. In this model, the SW speed varies with time and heliolatitude but is constant with the solar distance, and the SW density and the photoionization rate drop with the square of distance to the Sun and vary with heliolatitude and time (see Figure 20 in Sokół et al. 2013). The ionization model is described in Sokół et al. (2019a).

4. Acceleration of PUIs at the TS and the Energetic Ion Spectra

To simulate the proton distribution in the heliosheath, we invoke the mechanism proposed by Zank et al. (1996) and independently by Lee et al. (1996). The energized ions derive from PUIs arriving at the TS. The ions with a high enough perpendicular velocity component overcome the electrostatic potential barrier at the shock and are transmitted downstream. The remaining ones are initially reflected from the shock and spend some time drifting along the shock surface while gaining energy before ultimately crossing the shock downstream.

The shock strengths along the TS were scaled by a factor of 0.68 relative to the Huntsville simulation results. The scale factor was chosen via the requirement that the (rescaled) shock strength at the point where the model TS is crossed by *Voyager*

2 trajectory is equal to the value measured by *Voyager* 2. The result is similar to the subshock strength, predicted by models of the TS that incorporate distinct anomalous cosmic ray (ACR) and PUI components (Donohue & Zank 1993; Florinski et al. 2009).

Note that the MHD-kinetic model we use includes neither the ACR nor the PUI component as explicit separate fluids. Were the ACRs included along with their spatial diffusion coefficient, the overall shock would be mediated quite significantly and an extended smooth foreshock would be present (Donohue & Zank 1993; Florinski et al. 2009; Zank 2015). The important point here is that the actual shock with which the PUIs interact will be much weaker than given in the MHD and MHD-kinetic models, because these models simply identify the total jump, which includes the ACR foreshock contribution as well.

Following Zank et al. (1996, 2010), we estimated the fractions of the transmitted and reflected ion populations, as well as their average energies. We assumed a simple "filled shell" distribution for the PUIs upstream from the shock; see Equation (1) in Zank et al. (2010). To estimate the fractions of transmitted and reflected ions, we used the formula for the critical velocity for specular reflection from Equation (8) of Zank et al. (1996), and Equations (11a) and (11b) from Zank et al. (2010). To calculate the critical velocity for specular reflection, we used the radial component of magnetic field at 1 au equal to 30.0 μG, similar to that used in the Huntsville model, and we calculated the local magnetic field vector assuming the Parker spiral. Taking 37.5 μG does not lead to any significant changes.

Average energies of the transmitted and reflected ions were taken from Equations (8) and (10) of Zank et al. (2010). Since we do not know the $L_{\rm ramp}$ magnitude along the TS, we replaced it with the local values of the ion inertial length, which were determined based on local values of plasma density taken from the Huntsville simulation. The temperature of the bulk SW downstream of TS was set to 2×10^5 K, in agreement with *Voyager* observations (Richardson 2008). This approach correctly reproduces the observation from *Voyager* 2 during its TS crossing (see Figure 2).

The ion spectrum downstream was modeled as Maxwellian distributions for the bulk SW and transmitted ions, and a kappa function for the reflected ions, with the number densities and average energy values predicted by the abovementioned formulas from Zank et al. (1996, 2010). At each location along the TS where these formulas were used, we took appropriate plasma parameters from the Huntsville model simulation. The shock strength values were multiplied by the scale factor. For the kappa function, we used the value $\kappa = 1.6$, which is the approximate slope of the TS particle distributions observed by *Voyagers* (Decker et al. 2005). The PUI densities along the TS were calculated as described in Section 3 (Figure 1).

5. Generation of ENAs and Their Transport to 1 au

We assumed that the parent ions for the ENAs are transported from the TS by convection along the plasma flow lines. To calculate the ENA flux arriving at 1 au from a given direction, we considered a segment of the radially directed line of sight (LOS) between the TS and the HP or the outer boundary of 988 au. For a set of points along this LOS, we determined the plasma flow line that links this point with the initial point at the TS. The plasma flow lines and plasma

densities were taken from the global MHD-kinetic simulation. For a selected value of the ENA energy in the observer's frame, we found the parent ion velocities relative to the plasma for each point along the LOS. Subsequently, moving backward along the flow line, we determined the parent ion velocities at the initial point at the TS. This determination takes into account adiabatic acceleration of ions along the flow line. The amount of adiabatic acceleration was obtained based on the plasma density distribution along the flow line. We did not assess this acceleration from divergence of the flow, to avoid calculating numerical derivatives on a relatively sparse grid and the singularity at the shock.

With the ion velocity at the TS calculated, we computed the values of the energetic ion flux implied by our model spectrum at the TS. Simultaneously, we determined the loss factor for these energetic ions during their convection along the flow lines due to their neutralization via charge exchange with the ambient ISN hydrogen. The density and velocity of the background ISN hydrogen are taken from the Huntsville model. The velocity-dependent charge exchange cross section was adopted from Lindsay & Stebbings (2005). In this way, we determined the production rate of the ENAs moving toward the observer at selected points of the LOS. These production rates were subsequently integrated along the LOS to yield the ENA flux for this LOS. The losses to the ENAs on the way to the observer were not considered, because they are small for our energy range (Bzowski 2008; McComas et al. 2012), and we neglect any hypothetical production of ENAs inside the TS.

The results of our simulations of the ENA flux are shown in Figures 3 and 4.

6. ENA Flux Data

The ENA flux data used in this study consist of:

(1) The *IBEX* Hi globally distributed ENA flux, which is the flux obtained after removing the ribbon contribution. These data come from the period 2009 to 2014, and were published in Schwadron et al. (2014a). We used the flux data from the directions within $\pm 10°$ from the ecliptic plane, in the energy ranges 3–6 keV and (Figure 3 only) 2–3.8 keV.

(2) The HSTOF hydrogen ENA data obtained during the two first years of operation (1996–1997). This period of observations is unique because it combines high-quality observations with the coverage of all ecliptic longitudes. The HSTOF energy range is 58–88 keV.

HSTOF ENA observations were possible only during the quiet time periods, with low energetic ion flux. The years 1996 to 1997 included a large number of such periods. In 1998, connection with *SOHO* was temporarily lost. The subsequent four years had few quiet time periods. In the year 2003, *SOHO* was reoriented, with the result that the nose and tail ecliptic longitude sectors became inaccessible for HSTOF.

It should be noted that the first publication of the HSTOF ENH flux data (Hilchenbach et al. 1998) appeared before the in-flight calibration of the instrument, with the result that the flux was underestimated by about one order of magnitude, as outlined in Hilchenbach et al. (2001). The HSTOF data that we use here are derived from the recalibrated data, with a more stringent quiet-time flux threshold and resampled binning time periods

for the ENA flux averaging. These data were published in Hilchenbach et al. (2001), and for an extended period in Czechowski et al. (2006). In particular, a single high-flux data point near 0° ecliptic longitude shown in Hilchenbach et al. (1998) is absent from the present data, due to the revised data analysis, while several data points for H ENA fluxes emerging from the tail region are still present.

(3) The INCA ENA data in two energy bands (5.2–13.5 keV and 35–55 keV) have been digitized from Figure 3(a) in Dialynas et al. (2017). The data from INCA were collected between 2003 and 2014, with different regions in the sky observed at different times.

7. Results and Conclusions

Our main result (see Figures 3 and 4) is that the observed heliospheric ENA flux can be approximately reproduced, over a wide energy range, by a model combining the time-stationary conventional ("comet-like") model of the heliosphere with the model of the energetic proton spectrum based on the theory of Zank et al. (Figure 2). Over most of the energy range, our simulations give the right order of the ENA flux magnitude (except for INCA 5.2–13.5 keV data), and the directional (longitudinal) dependence of the ENA flux is similar to that observed by *IBEX* and HSTOF. The 5.2–13.5 keV INCA data have a longitudinal dependence similar to our simulations, but there is a discrepancy in flux magnitude by a factor of four.

We obtained this result without any parameter fitting; it is based solely on the parameter values available in the literature. In our opinion, we have obtained a good qualitative agreement between the data and observations. Therefore, even though the model we have used is a single-fluid plasma (albeit with the multicomponent distribution function), we believe these simplifications are of minor importance. Models including details such as effects of spatial diffusion of ions in the energy range of 5–100 keV are, to our knowledge, unavailable so far.

The bimodal nose-tail structure of the ENA flux (both simulated and observed) changes with increasing energy to a structure with one peak in the tail direction. For the simulated flux, this result is robust against various assumptions on the details of the PUI spectrum. In particular, the evolution of the bimodal structure is not affected by the adjustment of the shock strength parameter. Switching from the two-peak to the one-peak structure for the simulated flux occurs at ~20 keV (Figure 3). A similar behavior can be derived from a simple "toy" model (Appendix B). However, the INCA data have a bimodal structure both in the 5.2–13.5 keV and the 35–55 keV energy ranges (Figure 4). The single-peak structure is observed only by HSTOF (58–88 keV). Our interpretation is that switching to a single-peak structure in the ENA flux occurs at an energy higher than predicted by our simulations.

The simulated ENA flux is only weakly dependent on the solar phase (minimum or maximum). However, in each case, the simulation is based on the same stationary model of the heliosphere, such that the effect of the solar cycle on the global structure of the heliosphere is not taken into account.

Because we employed the time-stationary model of the heliosphere, we could not address the important question of time evolution of the energetic ions and the ENA fluxes observed during recent years. We have only considered the

effect of the solar cycle on pick-up proton distribution upstream of the TS (Figure 1).

In our simulations, we assume that the parent ions of the ENAs of different energies are convected with the same plasma flow, described by a single fluid that is a mixture of bulk SW and the PUIs. The question is whether the single-fluid description may offer an acceptable approximation. For example, if the core SW and different PUI components downstream from the TS were to be transported toward widely separated regions of the heliosheath, our approximation would be invalid, and our conclusions unsupported. We think, however, that this possibility is unlikely.

The main support for our opinion comes from observations by the *Voyager* 2 team (Richardson & Decker 2014, 2015; Decker et al. 2015). Most of the thermal pressure in the inner heliosheath is in the energy band 5.2–24 keV/nuc, which dominates the 5.2–3500 keV ion distribution (Dialynas et al. 2019). The agreement between the plasma velocity measurements by the plasma instrument Plasma Science on board *Voyager* 2 and the velocity estimations based on energetic particles anisotropy observed by LECP is consistent with the energetic particles being convected with the plasma flow for most of the observation period (2008–2014). The apparent discrepancy between the two observed in the 2009.3–2010.5 period can be explained as due to a contribution of heavy ions (Richardson & Decker 2014, 2015). The streaming of energetic ions occurs only during the period 2012.7–2013.3, which coincides with an abrupt fall in the intensity of the energetic ions (Richardson & Decker 2014, 2015; Decker et al. 2015). Our assumption that the plasma and the energetic particles flow together is, therefore, consistent with observations, with the exception of the short period during which the energetic particle flux is very low.

The differential flow between energetic ions of different energies might arise as a consequence of ion diffusion and drift in the heliosheath magnetic field. In the Huntsville model as well as our ENA simulation, the ion diffusion and drifts are neglected. This is consistent with the estimations by Florinski et al. (2009) and Mostafavi et al. (2017), which imply that the mean free paths for the ions in our energy range are much smaller than the size of the heliosheath. The differential flow does not then occur. To our knowledge, the available heliospheric models that include diffusion do not predict a qualitatively different structure of the heliosphere than do the standard models (Fahr et al. 2000; Scherer & Ferreira 2005; Malama et al. 2006; Guo et al. 2019).

Note that our ENA calculations do not assume that the spatial ion distributions are independent of energy. This is because we calculate the ion losses to neutralization along the plasma flow lines, starting from the TS, separately for each energy. In this way, our simulation goes beyond a single-fluid model.

Our simulations, and to some extent the observations, demonstrate that the ratio between the ENA flux from the tail and the nose directions is energy-dependent (Figures 3 and 4).

In the heliosphere with an extended tail, this can be understood as a consequence of the energy dependence of the ENA production rate. The cross section for charge exchange between the energetic proton and the neutral hydrogen atom decreases rapidly with the collision energy (Lindsay & Stebbings 2005), by two orders of magnitude over the combined energy range of *IBEX*-Hi, INCA, and HSTOF (0.7 to 88 keV). Because of losses

by conversion into ENAs, the protons energized at and convected from the TS do not fill the inner heliosheath uniformly. The effective source region for the high-energy ENAs observed by HSTOF (58–88 keV, proton loss rate low) extends to larger distances from the TS than the source region for the lower-energy ENAs observed by INCA (5–55 keV). Therefore, the fraction of the heliotail ENAs in the INCA data is smaller than in the HSTOF data, which could be the reason for the difference between the observations by HSTOF (maximum ENA flux from the heliotail) and INCA (similar flux from the nose and tail directions). This qualitative argument has been positively verified using simplified comet-like models of the heliosphere (Czechowski et al. 2018), and further confirmed by the present simulation. The INCA 35–55 keV data and the HSTOF data show that the switch to the one-peak structure of the ENA flux occurs above ∼50 keV, while the Huntsville model-based calculation implies a lower threshold of ∼20 keV (Figures 3 and 4).

We interpret the ENA flux peak dominating at high energy as a signature of the heliotail. The peak appears not at the ∼75° "anti-nose" position, but rather is shifted to about 90°. This shift is visible both in the simulation and in the ENA data from HSTOF. In the simulation, it reflects the interstellar magnetic field direction, which is inclined at ∼40° relative to the direction of the solar motion.

An alternative to the "comet-like" heliosphere may emerge in the limit of a strong interstellar magnetic field, when the magnetic pressure dominates the ram and thermal pressures. According to one of the models proposed by Parker (1961), the heliosheath outflow forms two tubes parallel and antiparallel to the interstellar magnetic field, and the downwind tail is missing. However, this type of the heliospheric structure is only confirmed by numerical simulations where the interstellar magnetic field direction happens to be parallel to the solar motion (Florinski et al. 2004; Pogorelov et al. 2011), or the Sun happens to be at rest relative to the interstellar medium (Czechowski & Grygorczuk 2017) (see Appendix C).

Observations of ENAs over energies 5.2–55 keV from INCA on the *Cassini* mission have shown rapid 2–3 yr time variations (Dialynas et al. 2017), which appear roughly correlated with the solar cycle. These 2–3 yr time variations observed by INCA are interpreted as requiring an LOS that is limited by the size of the heliosheath. Since the observed variations of ENAs from all directions seem to be correlated in time, the shape of the heliosphere is argued to be spheroidal (i.e., round). Like the "two-funnel" heliosphere, this round heliosphere represents a significant departure from a comet-like shape.

However, the interpretation of INCA data relies heavily on approximate equality between the upwind and downwind ENA flux intensity values, as well as the correlation between time variations of ENA fluxes from the upwind and downwind regions (Dialynas et al. 2017), which we have found to be consistent with a comet-like shape. Our simulations (Figures 3 and 4) show that the upwind and downwind ENA fluxes are, in fact, approximately equal to each other in the comet-like heliosphere, provided that the ENA energy is low enough. The time correlation between them can be explained within the comet-like paradigm of the heliosphere (Schwadron & Bzowski 2018). According to this explanation, the correlation is a consequence of time variations within the inner heliosheath driven by ram pressure changes in the SW and episodic cooling and heating of the inner-heliosheath plasma during the intervals of large-scale expansion and compression.

We conclude that the available observations of the directional distribution of the heliospheric ENA are qualitatively consistent with a comet-like structure of the heliosphere, of which the Huntsville model is an example. The approximate symmetry between the nose and the heliotail direction of ENA fluxes at energies up to several tens of keV is naturally explained by the decreasing magnitude of charge exchange cross section with energy. For increasing ENA energy, the tail-to-nose flux ratio is expected to increase. The future observations of very high-energy ENA (up to ∼500 keV) by IMAP Ultra (McComas et al. 2018) may, therefore, provide a crucial test of the existence of the heliotail. The agreement between our model results and the actual observed ENA fluxes over a wide energy range (from a few keV to almost 100 keV) supports the scenario where the PUIs reflected, accelerated, and transmitted at the TS, as proposed by Zank et al. (1996), Zank et al. (2010), Lee et al. (1996), are indeed the source of the heliospheric ENAs.

Appendix A
Parameter Values for the Simulation of the Global Heliosphere and the PUI Density at the TS

In this appendix, we demonstrate that parameter values adopted in the modeling are used consistently throughout the entire simulation process—starting from the unperturbed VLISM at the interstellar side, and SW and solar EUV output at the solar side—and that they were chosen based on published up-to-date measurement values.

A.1. Parameters of the Very Local Interstellar Medium Obtained from Heliospheric Observations

The velocity of the Sun relative to the VLISM, i.e., the inflow velocity of interstellar matter on the heliosphere, and the VLISM temperature were adopted based on analysis of interstellar helium observations compiled by McComas et al. (2015) ($T = 7500$ K, $v = 25.4$ km s^{-1}, ecliptic longitude 255°7, ecliptic latitude 5°1). The magnitudes of these quantities are based on analysis of direct-sampling observations by *IBEX*-Lo from 2009 to 2014 (Bzowski et al. 2015; Möbius et al. 2015a; Schwadron et al. 2015). These analyses do not rely on any particular model of the heliosphere and are based on the ballistics of neutral He atoms inside the heliosphere and a realistic model of ionization losses of interstellar He atoms inside the heliosphere. It is assumed that neutral He, H, and the plasma in the VLISM are in equilibrium. This assumption has been commonly made in heliospheric physics. The temperature and flow velocity of the VLISM we used are robust against independent analyses of observations from Ulysses (Bzowski et al. 2014; Wood et al. 2015) and the inflow direction obtained from PUI observations (Gloeckler et al. 2004; Möbius et al. 2015b).

The density of ISN H at the upwind point of the TS was obtained based on two independent estimates: (1) the magnitude of slowdown of the SW expansion speed due to mass loading by charge exchange with ISN H, observed in situ by *Voyager* 2 (Richardson et al. 2008), and (2) in situ measurement by Ulysses of the production rate of PUIs at the boundary of the density cavity of ISN H (Bzowski et al. 2008). It has been shown by Bzowski et al. (2009) that these estimates agree within mutual error bars. These authors suggested that the density of ISN H at the nose of the TS is 0.09 cm^{-3}. With this, based on global MHD-kinetic modeling of the heliosphere done using the Moscow MC Model (Izmodenov et al. 2003), the density of neutral H in the VLISM was estimated at 0.16 cm^{-3}, and the electron density $\sim$0.06 cm^{-3}.

The directions of inflow of the primary and secondary populations of ISN H were adopted in agreement with those for the primary and secondary populations of ISN He. The densities of these populations at the TS were adopted based on analysis of PUIs observed by Ulysses (Bzowski et al. 2008). The magnitudes of the parameters of the primary and secondary populations of ISN H we used are adopted after Kowalska-Leszczynska et al. (2018b).

The directions of inflow of the primary and secondary populations define the so-called neutral gas deflection plane (NDP). Heliospheric models suggest that the direction of inflow of the secondary population of neutral interstellar gas is located within the plane defined by the vectors of the Sun's motion through the VLISM and the interstellar magnetic field (the B-V plane). The NDP found from observations of interstellar He (see Figure 7 in Kubiak et al. 2016) agrees very well with the B-V plane found from fitting the Ribbon size and location (Zirnstein et al. 2016). In the present simulation of the heliosphere, we used the parameters obtained by these authors, listed in their Table 3 for the case of VLISM *B* field 3 μG. For the *B* field, we used the direction and strength reported by these authors as resulting from ribbon fitting, i.e., $B = 2.93\,\mu$G, $\lambda_B = 227°.28$, $\beta_B = 34°.62$ at 1000 au ahead of the Sun. This vector is in agreement with an independent determination (Frisch et al. 2015) based on examination of the direction of polarization of starlight on interstellar dust grains.

A.2. SW and EUV Conditions in the Heliosphere and the Sources of Information on Them

The parameters of the SW and solar EUV output used in the modeling of ISN H and PUIs were based on measurements (see Section 1).

The model of SW speed and density during the solar cycle was adopted based on interplanetary scintillation observations outside the ecliptic plane (Tokumaru et al. 2010, 2012), available from 1985, and within the ecliptic plane on in situ data from the OMNI collection (King & Papitashvili 2005), compiled into a homogeneous model (Bzowski et al. 2013b; Sokół et al. 2013). The SW density variations with heliolatitude were calculated based on a linear correlation between speed and densities at various latitudes, obtained from Ulysses in situ observations (Sokół et al. 2013) and the SW latitudinal invariant, as described in Le Chat et al. (2012) and Sokół et al. (2015). The photoionization rate was defined in Equations (3.23)–(3.25) of Bzowski et al. (2013b), based on EUV observations of the Sun and a system of solar proxies. The electron-impact ionization rate (important only within $\sim$1.5 au from the Sun) was adopted from Bzowski et al. (2013b).

The radiation pressure model was adopted from Equation (14) and Table 1 in Kowalska-Leszczynska et al. (2018a). The model was based on observations of the solar Lyα line profile during the solar cycle (Lemaire et al. 2005) and the total irradiance in the Lyα line, available from the LASP Composite Line-Averaged Solar Lyα flux (Woods et al. 2000). In this model, the resonant radiation pressure acting on H atoms varies with time, heliolatitude, and atom radial velocity.

These solar factors are calculated on a homogeneous time grid, with averaging over Carrington period, as well as on a homogeneous heliolatitude grid. The nWTPM model tracks individual atoms from a given location inside TS out to TS, and the solar factors are calculated along the trajectory, with their variation in time and with heliolatitude calculated by linear interpolation between the time and heliolatitude nodes.

Appendix B
Why the Nose/Tail ENA Flux Ratio Is Energy-dependent: The Toy Model

A simple "toy" model of energetic ion distribution and production of ENAs in the heliosphere was proposed by Czechowski et al. (2018). Since the model offers a simple explanation for the energy dependence of the nose-tail ENA flux asymmetry in a "comet-like" heliosphere, a brief description is included here. Two directions are considered: the stagnation line (the "nose") and the center of the "tail." The ion distribution $J(z)$ along these directions is calculated taking into account the plasma convection toward the nose (plasma speed $V(z) = V_0(1 - z/L)$) and toward the tail (assuming plasma speed $V = $ const), as well as the neutralization losses (with the loss rate β_{cx}). The ENA flux from the nose direction is then

$$J_{\text{ENA,nose}} = \frac{\beta_{cx}L}{\beta_{cx}L + V_0}\frac{V_0}{v}J_{0,\text{nose}}, \qquad (4)$$

and that from the tail is

$$J_{\text{ENA,tail}} = \frac{V}{v}J_{0,\text{tail}}, \qquad (5)$$

where v is the speed of the ENA, V the plasma speed in the tail, and $J_{0,\text{nose}}$ and $J_{0,\text{tail}}$ are the energetic ion densities at TS in the respective directions.

Assuming $L = 25$ au, $V_{0,\text{nose}} = 100$ km s^{-1}, $V_{\text{tail}} = 26$ km s^{-1}, and $J_{0,\text{nose}}/J_{0,\text{tail}} = 2$ (to account for the asymmetry of the TS), and taking the loss rate $\beta_{cx} = \sigma_{cx}\,n_H\,v$, where the ISN density $n_H = 0.1$ cm^{-3} and the charge-exchange cross section σ_{cx} is given by the formula of Lindsay & Stebbings (2005), it follows that the ENA tail/nose flux at ratio 1 au is 1.6 at the ENA energy 58 keV (the lowest HSTOF value) and becomes 1 at 46 keV (the midpoint of the highest INCA energy bin).
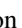
Appendix C
MHD Model of Parker Solution for the Heliosphere for the Strong Interstellar Magnetic Field

Available observations suggest that, with the observed magnitudes of the plasma and magnetic field parameters in the VLISM, the dominant component of the pressure balance is the ram pressure, not the magnetic pressure (Schwadron & Bzowski 2018), although the magnetic pressure is high enough to cause some tilt and deformation of the heliotail. MHD models of the heliosphere are capable of reproducing solutions close to that

presented in Figure 3 in the classical paper (Parker 1961), provided that plasma flow velocity is almost nil (Czechowski & Grygorczuk 2017, Figure 2) or directed parallel to the magnetic field direction (Florinski et al. 2004; Pogorelov et al. 2011). For inflow velocities not parallel to the magnetic field, such as those obtained from analysis of neutral interstellar gas observations (20–25 km s^{-1}), and a very strong magnetic field of 20 μG, the model of Czechowski & Grygorczuk (2017) predicts the plasma outflow to be mostly concentrated along two close-to-antiparallel funnels, but a heliotail is nevertheless present. The two-funnel structure gradually disappears for a magnetic field strength decreasing toward the values available from observations; e.g., for 5 μG in the unperturbed VLISM, the funnels are absent (Czechowski & Grygorczuk 2017, Figure 4).

ORCID iDs

A. Czechowski https://orcid.org/0000-0002-4441-5377
M. Bzowski https://orcid.org/0000-0003-3957-2359
J. M. Sokół https://orcid.org/0000-0002-4173-3601
J. Heerikhuisen https://orcid.org/0000-0001-7867-3633
E. J. Zirnstein https://orcid.org/0000-0001-7240-0618
N. V. Pogorelov https://orcid.org/0000-0002-6409-2392
N. A. Schwadron https://orcid.org/0000-0002-3737-9283
M. Hilchenbach https://orcid.org/0000-0003-1703-7777
J. Grygorczuk https://orcid.org/0000-0003-3951-0043
G. P. Zank https://orcid.org/0000-0002-4642-6192

References

Baranov, V. B., Izmodenov, V. V., & Malama, Y. G. 1998, JGR, 103, 9575
Baranov, V. B., Lebedev, M. G., & Malama, Y. G. 1991, ApJ, 375, 347
Bzowski, M. 2003, A&A, 408, 1155
Bzowski, M. 2008, A&A, 488, 1057
Bzowski, M., Kubiak, M. A., Hłond, M., et al. 2014, A&A, 569, A8
Bzowski, M., Möbius, E., Tarnopolski, S., Izmodenov, V., & Gloeckler, G. 2008, A&A, 491, 7
Bzowski, M., Möbius, E., Tarnopolski, S., Izmodenov, V., & Gloeckler, G. 2009, SSRv, 143, 177
Bzowski, M., Sokół, J. M., Kubiak, M. A., & Kucharek, H. 2013a, A&A, 557, A50
Bzowski, M., Sokół, J. M., Tokumaru, M., et al. 2013b, in Cross-Calibration of Far UV Spectra of Solar Objects and the Heliosphere, ed. E. Quémerais, M. Snow, & R. Bonnet (New York: Springer Science+Business Media), 67
Bzowski, M., Swaczyna, P., Kubiak, M. A., et al. 2015, ApJS, 220, 28
Czechowski, A., & Grygorczuk, J. 2017, JPhCS, 900, 012004
Czechowski, A., Hilchenbach, M., Hsieh, K. C., et al. 2018, A&A, 618, A26
Czechowski, A., Hilchenbach, M., & Kallenbach, R. 2006, ISSIR, 5, 311
Decker, R. B., Krimigis, S. M., Roelof, E. C., et al. 2005, Sci, 309, 2020
Decker, R. B., Krimigis, S. M., Roelof, E. C., & Hill, M. E. 2015, JPhCS, 577, 012006
Dialynas, K., Krimigis, S. M., Decker, R. B., & Mitchell, D. G. 2019, GeoRL, 46, 7911
Dialynas, K., Krimigis, S. M., Mitchell, D. G., Decker, R. B., & Roelof, E. C. 2017, NatAs, 1, 0115
Donohue, D. J., & Zank, G. P. 1993, JGR, 98, 19005
Fahr, H. J., Kausch, T., & Scherer, H. 2000, A&A, 357, 268
Florinski, V., Decker, R. B., le Roux, J. A., & Zank, G. P. 2009, GeoRL, 36, L12101
Florinski, V., Pogorelov, N. V., Zank, G. P., Wood, B. E., & Cox, D. P. 2004, ApJ, 604, 700
Frisch, P. C., Berdyugin, A., Piirola, V., et al. 2015, ApJ, 814, 112

Giacalone, J., & Decker, R. 2010, ApJ, 710, 91
Gloeckler, G., Allegrini, F., Elliott, H. A., et al. 2004, ApJL, 604, L121
Gruntman, M. A. 1997, RScI, 68, 3617
Guo, X., Florinski, V., & Wang, C. 2019, ApJ, 879, 87
Heerikhuisen, J., & Pogorelov, N. V. 2010, in ASP Conf. Ser. 429, Numerical Modeling of Space Plasma Flows, Astronum-2009, ed. N. V. Pogorelov, E. Audit, & G. P. Zank (San Francisco, CA: ASP), 227
Hilchenbach, M., Hsieh, K. C., Hovestadt, D., et al. 1998, ApJ, 503, 916
Hilchenbach, M., Hsieh, K. C., Hovestadt, D., et al. 2001, in The Outer Heliosphere: The Next Frontiers, ed. K. Scherer et al. (Amsterdam: Pergamon), 273
Holzer, T. E., & Axford, W. I. 1971, JGR, 76, 6965
Izmodenov, V., Malama, Y. G., Gloeckler, G., & Geiss, J. 2003, ApJL, 594, L59
King, J. H., & Papitashvili, N. E. 2005, JGRA, 110, A02104
Kowalska-Leszczynska, I., Bzowski, M., Sokół, J. M., & Kubiak, M. A. 2018a, ApJ, 852, 15
Kowalska-Leszczynska, I., Bzowski, M., Sokół, J. M., & Kubiak, M. A. 2018b, ApJ, 868, 49
Kubiak, M. A., Swaczyna, P., Bzowski, M., et al. 2016, ApJS, 223, 25
Kumar, R., Zirnstein, E. J., & Spitkovsky, A. 2018, ApJ, 860, 156
Le Chat, G., Issautier, K., & Meyer-Vernet, N. 2012, SoPh, 279, 197
Lee, M. A., Shapiro, V. D., & Sagdeev, R. Z. 1996, JGR, 101, 4777
Lemaire, P., Emerich, C., Vial, J.-C., et al. 2005, AdSpR, 35, 384
Lindsay, B. G., & Stebbings, R. F. 2005, JGR, 110, A12213
Malama, Y., Izmodenov, V. V., & Chalov, S. V. 2006, A&A, 445, 693
McComas, D., Bzowski, M., Fuselier, S., et al. 2015, ApJS, 220, 22
McComas, D. J., Dayeh, M. A., Allegrini, F., et al. 2012, ApJS, 203, 1
McComas, D. J., Dayeh, M. A., Funsten, H. O., et al. 2018, ApJL, 856, L10
Möbius, E., Bzowski, M., Fuselier, S. A., et al. 2015a, ApJS, 220, 24
Möbius, E., Lee, M. A., & Drews, C. 2015b, ApJ, 815, 20
Mostafavi, P., Zank, G. P., & Webb, G. M. 2017, ApJ, 841, 4
Parker, E. N. 1961, ApJ, 134, 20
Pogorelov, N. V., Heerikhuisen, J., Zank, G. P., et al. 2011, ApJ, 742, 104
Pogorelov, N. V., Zank, G. P., Borovikov, S. N., et al. 2008, in ASP Conf. Ser. 385, Numerical Modeling of Space Plasma Flows, ed. N. V. Pogorelov, E. Audit, & G. P. Zank (San Francisco, CA: ASP), 180
Richardson, J. D. 2008, GeoRL, 35, 23104
Richardson, J. D., & Decker, R. B. 2014, ApJ, 792, 126
Richardson, J. D., & Decker, R. B. 2015, JPhCS, 577, 012021
Richardson, J. D., Liu, Y., Wang, C., & McComas, D. 2008, A&A, 491, 1
Ruciński, D., & Bzowski, M. 1995, A&A, 296, 248
Ruciński, D., Bzowski, M., & Fahr, H. J. 2003, AnGeo, 21, 1315
Ruciński, D., & Fahr, H. J. 1991, AnGeo, 9, 102
Scherer, K., & Ferreira, S. 2005, ASTRA, 1, 17
Schwadron, N., Möbius, E., Leonard, T., et al. 2015, ApJS, 220, 25
Schwadron, N. A., Adams, F. C., Christian, E. R., et al. 2014a, Sci, 343, 988
Schwadron, N. A., & Bzowski, M. 2018, ApJ, 862, 11
Schwadron, N. A., Moebius, E., Fuselier, S., et al. 2014b, ApJS, 215, 13
Sokół, J. M., Bzowski, M., & Tokumaru, M. 2019a, ApJ, 872, 57
Sokół, J. M., Bzowski, M., Tokumaru, M., Fujiki, K., & McComas, D. J. 2013, SoPh, 285, 167
Sokół, J. M., Kubiak, M. A., & Bzowski, M. 2019b, ApJ, 879, 24
Sokół, J. M., Swaczyna, P., Bzowski, M., & Tokumaru, M. 2015, SoPh, 290, 2589
Tarnopolski, S., & Bzowski, M. 2009, A&A, 493, 207
Thomas, G. E. 1978, AREPS, 6, 173
Tokumaru, M., Kojima, M., & Fujiki, K. 2010, JGR, 115, A04102
Tokumaru, M., Kojima, M., & Fujiki, K. 2012, JGRA, 117, A06108
Vasyliunas, V., & Siscoe, G. 1976, JGR, 81, 1247
Wood, B. E., Müller, H.-R., & Witte, M. 2015, ApJ, 801, 62
Woods, T. N., Tobiska, W. K., Rottman, G. J., & Worden, J. R. 2000, JGR, 105, 27195
Zank, G., Heerikhuisen, J., Pogorelov, N., Burrows, R., & McComas, D. 2010, ApJ, 708, 1092
Zank, G. P. 2015, ARA&A, 53, 449
Zank, G. P., Pauls, H. L., Cairns, I. H., & Webb, G. M. 1996, JGR, 101, 457
Zirnstein, E. J., Heerikhuisen, J., Funsten, H. O., et al. 2016, ApJL, 818, L18